Photodegradation of Ciprofloxacin-Zinc Complexes Produced at the Interface of ZnO and Cu-Doped ZnO Crystals

Aryane Tofanello[a], Elisângela Belleti[a], Adrianne M. M. Brito[a] ⓘ *, Iseli L. Nantes-Cardoso[a]** ⓘ

[a]Universidade Federal do ABC, Centro de Ciências Naturais e Humanas, Av. dos Estados, 5001, 09210-580, Santo André, SP, Brasil.

Ciprofloxacin hydrochloride (CIPRO) is considered an emerging pollutant in aquatic environments with the capacity to disseminate antibiotic resistance. Considering the pro-oxidant potential of ZnO and Cu-doped ZnO (Cu-ZnO) wurtzite crystals, the potential Ciprofloxacin photodegradation by these materials was investigated. CIPRO titration with ZnO and Cu-ZnO promoted the formation of zinc complexes and ~4% antibiotic adsorption. The carboxylic groups of CIPRO can complex Zn^{2+} by promoting the nanoetching of ZnO and Cu-ZnO crystallite surfaces. The alkaline interfaces provided by ZnO create a microenvironment favorable for Zn^{2+} chelation by CIPRO carboxylates. The photodegradation degree was similar for CIPRO and CIPRO-Zn under UV light, as revealed by UV-visible spectroscopy and FTIR. Therefore, the ZnO and Cu-ZnO crystals contributed to the formation of CIPRO-Zn rather than the photo-oxidative degradation of the antibiotic. Considering that CIPRO-Zn chelates disfavor bacterial selection for resistance, the treatment of CIPRO-contaminated effluents with ZnO and Cu-ZnO can facilitate desirable metal chelation without impairing photodegradation.

Keywords: *Ciprofloxacin, emergent pollutant, photodegradation, ZnO, Cu-ZnO nanoetching.*

1. Introduction

Ciprofloxacin (CIPRO) is a third-generation fluoroquinolone antibiotic that is widely used to treat a broad variety of bacterial infections[1]. The chemical structure of CIPRO presents two ionizable functional groups, the 6-carboxylic group with pK_{a1} = 6.09 and the N-4 of the piperazine ring with pK_{a2} = 8.62, resulting in an isoelectric point (pI) of 7.14 (Figure 1)[2]. The occurrence of the intersystem crossing of the singlet electronically excited state of quinolones after light absorption is reported in literature[3-5]. Studies of Bani-Yaseen et al.[6] assigned quinolone moiety as responsible for most of fluoroquinolones properties of absorption and fluorescence spectra. Thus, the photoexcitation of CIPRO produces triplet excited states that can trigger reactions leading to photosensitivity in patients undergoing antibiotic treatment[7,8]. On the other hand, the photophysical properties of CIPRO are also involved in its photodegradation in diverse environments exposed to light[9,10]. The widespread use of CIPRO has promoted pollution in aquatic environments[11-13].

More recently, CIPRO residues have been found in agricultural effluents[11,14], home dirt[11,12,14], and urban water[15]. Concentrations of CIPRO detected in groundwater, surface water and seas vary from ng to mg/L^{-1}, which indicates a real risk to the environment and human health[16]. The biological decomposition of CIPRO is not favorable because of its complex and stable chemical structure[17]. Therefore, a crescent search for effective strategies for CIPRO removal and degradation has mobilized researchers worldwide. The use of semiconductors for the photodegradation of

organic compounds has received considerable attention due to their potential for commercialization towards the environmental purification, optical applications, treatment of papermaking wastewater, in the field of cosmetology, antibacterial agent, and catalysts[18]. Most of them are highly active under UV/visible irradiation and therefore have considerable appeal in photocatalytic processes[19,20].

With the immediate necessity for effective degradation of the main organic environmental pollutants, semiconductor-assisted photocatalysis has become extremely appropriate and advantageous. The strategy consists of employing a semiconductor metal oxide or one of its doped variants as a strong oxidizing agent, which after irradiation charges up and leads to the generation of highly reactive oxidative species for the remediation of organic pollutants through advanced oxidation processes (AOPs)[21]. AOPs are based on the *in situ* production of reactive hydroxyl radicals (•OH) at the solid-liquid interface with an effective and non-selective oxidizing capacity, which are responsible for generating electron/hole pairs with the ability to degrade most organic pollutants[22,23]. Most of them are anchored on the oxide surface and are responsible for generating electron/hole pairs with the ability to degrade most organic pollutants[21]. The initial interaction of •OH sets off a sequence of oxidation reactions, which finally results in the mineralization of the target pollutant. ZnO has been reported as an appropriate catalyst for the mineralization of organic pollutants because of its well-known capacity to produce, under irradiation, oxidative species such as OH•, superoxide ions ($O_2^{-•}$), hydrogen peroxide (H_2O_2), and singlet oxygen ($^1\Delta_g O_2$)[24-30].
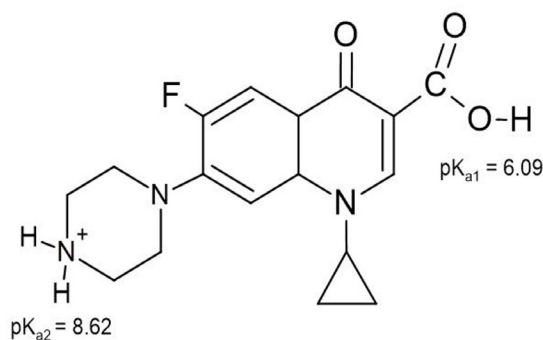
Figure 1. Chemical structure of CIPRO molecule with its ionizable groups and indication of the respective pK_a values.

ZnO has chemical stability, considerable oxidation efficiency, low toxicity, low production cost, and easy availability and applicability. Thus, the choice of ZnO as a representative II–VI group semiconductor is justified by its wide bandgap ($E_g = 3.37$ eV), which guarantees high oxidizing capacity, pronounced photosensitivity, and environmentally safe nature[31]. Together, these characteristics make ZnO a suitable photocatalyst for the treatment of organic wastewater by removing or dissolving organic compounds and solutions to environmental pollution problems[32]. It is well known that the doping of metal oxides with transition metal ions can potentiate the crystal defects that induce recombination processes and affect the optical properties, shifting the optical absorption toward the solar region. An alternative route of modifying the absorption and emission in the visible region is by doping the ZnO structure with copper ions[33,34]. In this study, pure and doped ZnO 1D architectures were synthesized using the hydrothermal method and their photocatalytic responses were explored in the decomposition of CIPRO.

2. Materials and Methods

2.1. Chemicals

All chemicals used in this study were of analytical grade and were used without further purification from Sigma-Aldrich. Ciprofloxacin hydrochloride salt (500 mg), a commercially available soluble form used in clinical applications, is commercially available.

2.2. Synthesis of ZnO and Cu-ZnO photocatalysts

Based on a facile hydrothermal synthesis procedure[35] 1.14 g $ZnCl_2$ (Sigma Aldrich, ACS reagent ≥98%) was dissolved in 80 mL of deionized water. Then, 4 mL of 30% ammonium hydroxide solution was added under magnetic stirring. In the next step, the white milky solution was transferred into a Schott bottle, maintained at 120 °C for 6 h in an oven and then cooled to room temperature naturally. Finally, the white product (ZnO) was washed with deionized water and ethanol and dried at 60 °C for a few hours[35]. With the same experimental procedure as above, Cu-dopped ZnO was manufactured by adding 1.08 g $ZnCl_2$ and 0.06 g of $CuSO_4 \cdot 5H_2O$ (Sigma Aldrich, ACS reagent ≥98%) as precursor aqueous solution. After the hydrothermal step, the blue light powder was washed and dried. More details about

the crystal growing (Figure S1) and equations are detailed in the Supplementary Material.

2.3. Characterization

The crystal phase and crystallinity of the photocatalysts were investigated using an X-ray diffractometer (Bruker D8 Discover XRD system) with MoKα1 radiation ($\lambda = 0.07093$ nm). The Fourier transform infrared (FTIR) spectra of the CIPRO samples were recorded between 4000 and 400 cm^{-1} using a 640-IR FTIR spectrometer from Agilent Technologies. The surface zeta potentials were measured using a Zetasizer Nano ZS from Malvern Panalytical. Scanning electron microscopy (SEM) images were obtained using a JSM-6010 microscope from JEOL operated at an acceleration voltage of 10 kV. Ultraviolet-visible (UV–vis) spectra were recorded using an Evolution 220 Thermo Fisher spectrophotometer.

2.4. Photocatalytic degradation

Previously to the photodegradation experiments, the solution of CIPRO was titrated with different masses of ZnO and Cu-ZnO to establish the spectral changes indicative of antibiotic-zinc oxide interaction detailed in the Supplementary Material. The photocatalytic degradation of the antibiotic was performed using 1.2-20 mg of the photocatalyst in 100 mL of Ciprofloxacin hydrochloride solution ($C = 6.0$ nmol L^{-1}) in deionized water. Before illumination, the systems containing the antibiotic and photocatalyst were maintained in the dark for at least 15 min to ensure the establishment of adsorption-desorption equilibrium. The samples were irradiated with a UV lamp at a fixed wavelength ($\lambda = 254$ nm) at 25 °C in deionized water. A compact 4W UVB lamp (UVGL-25 model, UVP Company, Upland, CA, USA) was used to irradiate the samples. The incident light intensity was established at 4 mW cm^{-2}, measured by a laser power meter model FieldMate with PowerMax thermal sensors at a distance of 4 cm^{36}. The degradation was monitored using UV-Vis spectroscopy every 60 min in the 800–200 nm range. photobleaching was analyzed by the temporal decrease in the absorbance bands and the differential spectra obtained by subtracting the final from the initial spectra.

The photodegradation was analyzed by UV-visible spectrophotometry and Fourier Transform Infrared (FTIR) detailed in the Supplementary Material.

3. Results and Discussion

To investigate the possible use of the pro-oxidant properties of zinc oxide materials to promote CIPRO photodegradation, two syntheses were performed: ZnO and Cu-ZnO. The morphologies of the as-synthesized ZnO and Cu-ZnO photocatalysts were characterized using scanning electron microscopy (SEM). Figure 2A-D shows the profile of the oxide crystals, which consist of rice grain-like structures with two sharp tips. The rice grain-like ZnO microrods exhibit a length of 5.25 ± 0.61 μm and a width of 1.20 ± 0.11 μm, respectively. For the doped photocatalyst, the observed length was 7.30 ± 0.92 μm with a width of 1.30 ± 0.15 μm. In this case, doping was detrimental to controlling the size of the crystal, in which small nuclei can spontaneously grow into
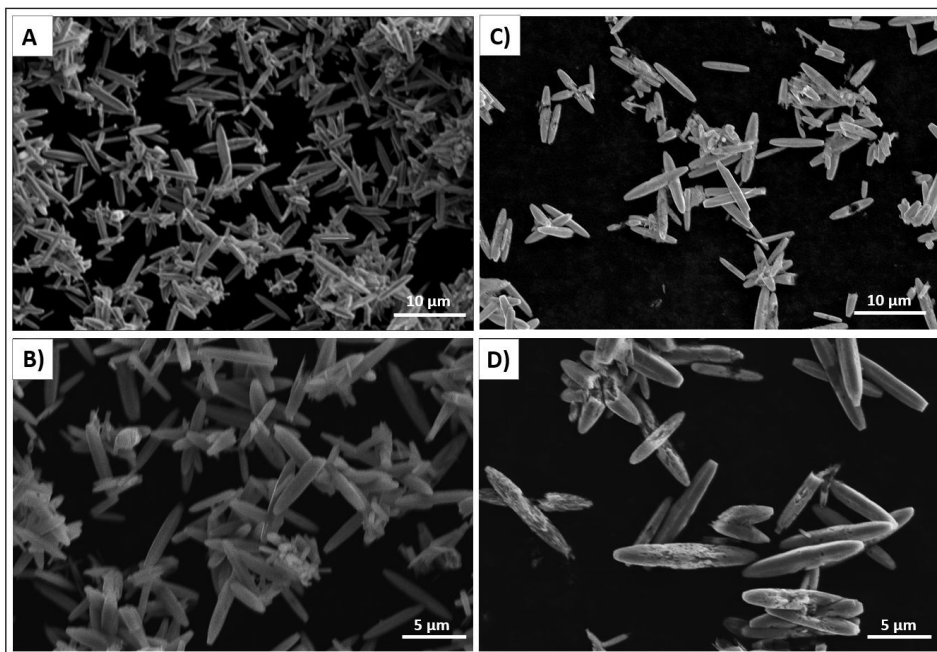
Figure 2. Scanning electron microscope images of ZnO (A) and (B) and Cu-ZnO microcrystals (C) and (D).
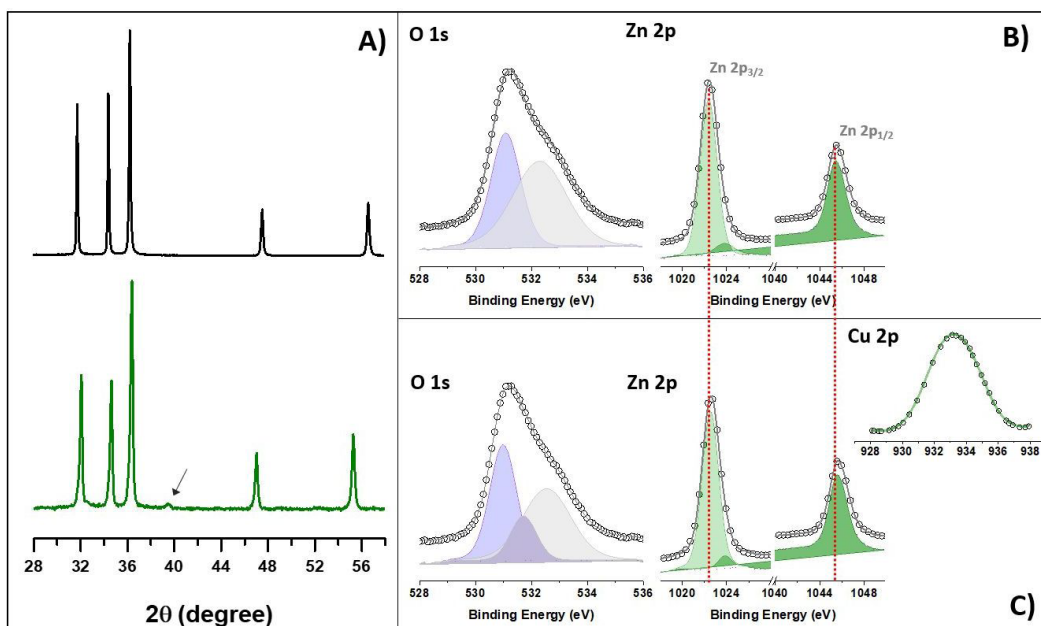

Figure 3. Structural characterization of ZnO and Cu-ZnO. A) X-ray diffraction of ZnO; B) XPS spectra of O1s, Zn2p of ZnO and C) XPS spectra of O1s, Zn2p of ZnO and Cu2p of Cu-ZnO.

larger particles. Doping with copper had an important effect on the photocatalyst morphology, inducing the appearance of small faults (surface defects) along the length of the rod, which became less homogeneous. Moreover, the incorporation of copper ions in the precursor solution altered the mechanisms governing the nucleation, growth, and ripening rates of ZnO, and further the incomplete growth of the 1D rods. This may be because the dopant insertion into the reaction environment

may have formed new Cu-Zn complexes, which may act as unwanted seeds for the subsequent controlled growth of rice grain-like ZnO microrods. This profile reveals that the incorporation of Cu into the ZnO lattice changed the oxide surface more significantly than its crystalline structure. In the sequence, the crystal structure of the as-prepared ZnO and Cu-ZnO photocatalysts was characterized by X-ray diffraction (XRD), as shown in Figure 3A. All reflection peaks can be

indexed to the standard hexagonal wurtzite ZnO by comparison with the data from JCPDS File No. 00-036-1451, indicating the high purity and crystallinity of the as-synthesized products[37]. Peaks located at 2θ = 31.82°, 34.44°, 36.30°, 47,57°, and 56.64°, were identified as corresponding to the (100), (002), (101), (102), and (110) planes for pure ZnO (Figure 3A black line). The secondary phase was not observed, and the cell parameters were a = 3.247 Å and c = 5.201 Å. No pronounced peaks corresponding to CuO or Cu_2O were observed in the as-synthesized Cu-ZnO using the hydrothermal route (Figure 3A, green line), except for the low-intensity diffraction peak at 39.1° belonging to the monoclinic phase CuO (centered base) indicated by the arrow[38]. The absence of Cu-related peaks rules out the existence of Cu-based clusters within the detection limit of XRD due to the low intentional incorporation caused by the synthesis method. After copper doping, the slight peak shift towards the larger 2θ angle in relation to the undoped ZnO is related to diffusion and consequently the replacement of Zn^{2+} ions in the lattice by Cu^{2+} ions without considerably altering the crystal structure, since both have similar ionic radii[39,40].

Thus, the diffraction pattern suggests that the main copper doping mechanism can be described by the interstitially Cu^{2+} inserted into the host lattice along with the reduced substitutional doping, as proposed in a previous work[38,41,42]. To reinforce this statement, the cell parameters did not change considerably and the maintenance of the crystallographic lattice indicated that the Cu-doped ZnO microstructure was not affected by the presence of intrinsic stress, attributed to impurities, defects or lattice distortions. The elemental compositions and surface chemistry of rice grain-like ZnO and Cu-ZnO were also studied using XPS analysis. The binding energies (BEs) in all the XPS spectra were calibrated using the binding energy of C 1s (284.8 eV). Signals of Zn 2p, Cu 2p and O 1 s from the ZnO surface were selected for investigation. Figures 3B and C show the comparative XPS spectra of the Zn $2p_{1/2}$ and Zn $2p_{2/3}$ core states of ZnO for both the pure and Cu-doped photocatalysts, respectively. The binding energies of Zn $2p_{3/2}$ and Zn $2p_{1/2}$ of rice grain-like ZnO microrods were 1022.4 eV and 1045.5 eV (corresponding to spin-orbit splitting of 23.1 eV), respectively, and are shown in Figure 3B. For the undoped ZnO, the main peak of Zn $2p_{3/2}$ was deconvoluted into two peaks at 1022.3 and 1023.8 eV. The contribution of the higher BE was ascribed to Zn^{2+} in the wurtzite ZnO structure, while the lowest intensity was related to Zn^{2+} in the hydroxide phase. Figure 3B also shows the relevant spectra for the O 1s peak for the ZnO rice grain-like microrods. The two significant peaks were observed at 531.1 eV and 532.3 eV for the undoped sample[43]. The first may be associated with the O^{2-} ions present in the oxygen-deficient regions within the ZnO structural lattice.

The other contribution is associated with weakly bonded oxygen chemically absorbed on the oxide surface during the formation process. The binding energies of the rice grain-like microrods are remarkably similar to the standard values of ZnO and are in good agreement with the oxidation state of Zn^{2+} in the wurtzite phase. To investigate the surface element composition and the chemical state of Cu insertion, XPS measurements were performed to further support our proposition on doped structure formation. The spectra confirmed the existence of Zn, Cu and O atom contributions

(Figure 3C). Figure 3C clearly shows that the peaks related to the binding energy of 1021.16 eV and 1044.26 eV were attributed for Zn $2p_{3/2}$ and Zn $2p_{1/2}$, respectively. For Cu-ZnO, both the Zn $2p_{1/2}$ and the Zn $2p_{3/2}$ peaks shift to higher energies by 0.16 eV in comparison with those for pure ZnO, according to the red line. The slight change in binding energies revealed that Cu doping partially replaced Zn^{2+} with Cu^{2+} in the ZnO lattice and the incorporation of Cu^{2+} ions into the ZnO lattice sites (Cu-O-Zn) may be inferred[41,44]. In the Cu 2p spectra, a prominent peak corresponding to the Cu $2p_{3/2}$ core level was observed at 933.3 eV, which was assigned to the cationic copper species (Cu^{2+} ions in the ZnO host material). Based on data from the literature, in the case of our doped photocatalyst, the divalent valence state of copper was predominant. In addition, there are other contributions that correspond to a mixed oxidation state of elemental Cu, which has already been observed in similar structures[43,45,46]. The divalent state of Cu was also supported by the XRD pattern, in which the peaks changed to higher angles owing to the smaller interplanar spacing[47]. The profile for O 1s was broad and asymmetrical, as shown in Figure 3C, which indicates the presence of multi-component oxygen species on the surface region, similar to the result exhibited by pure ZnO.

The two components, located at 531 eV and 531.7 eV, were attributed to oxygen in the Cu-ZnO crystalline lattice and the third peak at about 532.6 eV is associated with oxygen deficient regions in the ZnO arrangement. Accordingly, XPS analysis demonstrated the formation of pure and Cu-doped ZnO in the as-synthesized structures. After structural characterization of the ZnO and Cu-ZnO materials, their interactions with CIPRO were investigated. An aqueous solution of CIPRO (0.02 mg/mL) was titrated with ZnO and Cu-ZnO powder in the concentration range of 0.012 to 0.12 mg/mL.

Figures 4(A-E) and 4(F-J) show the spectral changes observed by the addition of increased amounts of ZnO and Cu-ZnO photocatalysts, respectively. Ciprofloxacin spectral changes were similar to those previously described by Muthumariappan, 2013 for the CIPRO-zinc complex[16]. The CIPRO absorbance spectrum exhibited peaks at 277, 317, and 330 nm. After titration completion, in which 0.12 mg/mL of ZnO and Cu-ZnO were present in the solution, the band at 277 nm showed a hypsochromic shift to 271 nm and the peaks at 317 and 330 nm were redshifted to 322 and 335 nm, respectively[6,48]. It was obtained the differential spectra for the complexes obtained using ZnO and Cu-ZnO by subtracting CIPRO spectrum from the spectra obtained after the addition of each incremental mass of ZnO microparticles. From the differential spectra, the plot of absorbance at 260 and 325 nm and the corresponding plot logA versus the microstructure mass revealed a two-step process of complexation. For the spectral changes promoted by the addition of ZnO and Cu-ZnO addition, a turning point of the complexes occurred at a microstructure concentration of 0.06 mg/mL. Considering that the spectra of CIPRO in the presence of ZnO and Cu-ZnO feature as CIPRO-Zn spectrum, the sample was centrifuged at 14,000 rpm to check the binding of CIPRO to ZnO materials. The supernatant spectrum showed that CIPRO binding to the microstructures was not favored because the CIPRO absorbance intensity decreased by only ~4.5% (Figure 5A). Considering that the ZnO microstructure was synthesized using
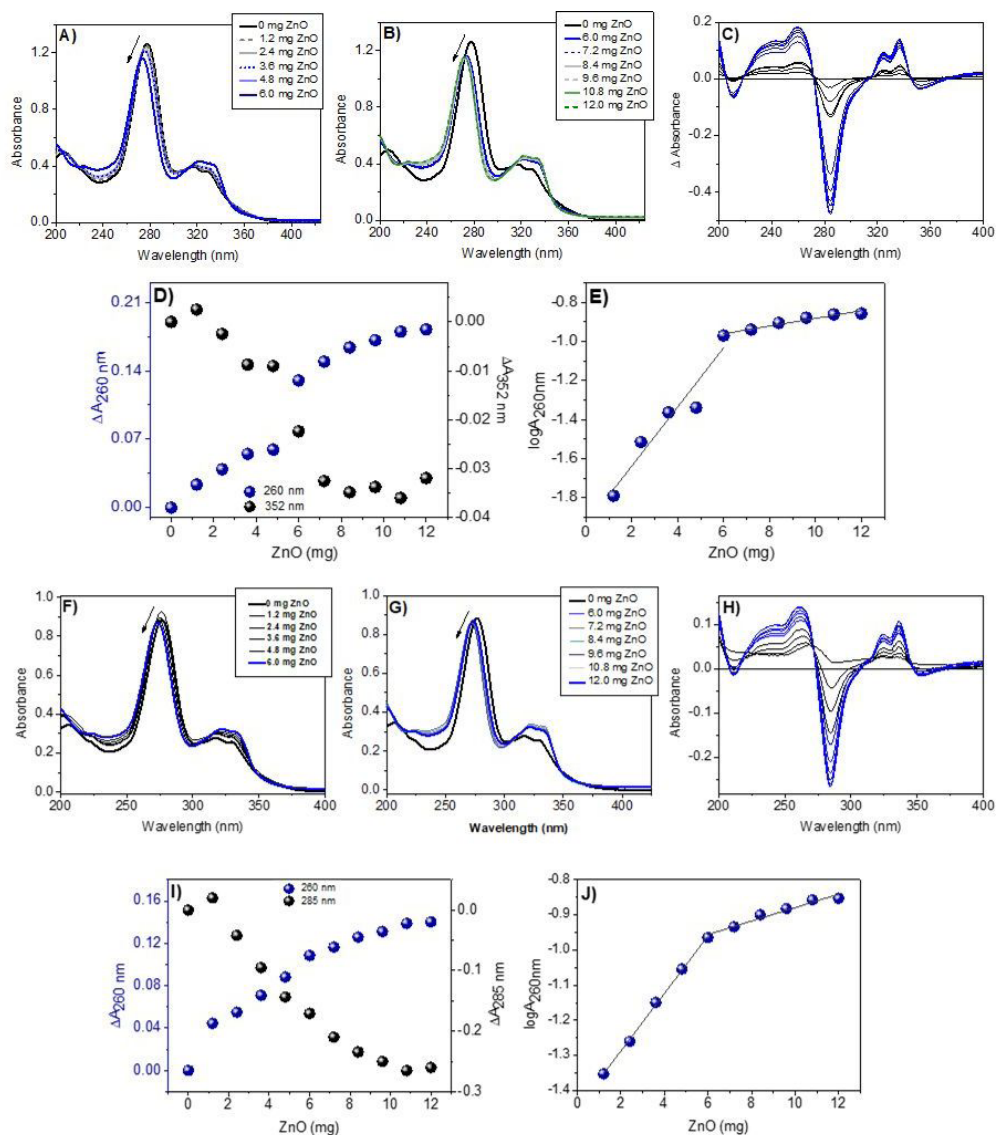
Figure 4. Changes in the CIPRO spectrum promoted by the interaction with ZnO and Cu-ZnO materials. A-B) and F-G) CIPRO photobleaching promoted by titration with ZnO and Cu-ZnO, respectively. The spectra obtained by titration with 0.012 to 0.06 mg/mL of ZnO and Cu-ZnO is shown in A and F, respectively, and B and G show the spectra obtained with 0.06 to 0.12 mg/ mL of ZnO and Cu-ZnO. C) and H) shows the corresponding differential spectra for ZnO and Cu-ZnO titration; D) and I) show the spectral changes at 260 and 285 nm and E) and J) the corresponding linearization by using $logA_{260\,nm}$.

$ZnCl_2$ as a precursor, the titration of CIPRO with the zinc salt was performed under the same conditions used for titration with ZnO, that is, in ultrapure water, at 25°C. Figure 5B shows the spectral changes obtained from the CIPRO (0.02 mg/mL) before and after the addition of $ZnCl_2$ (0.20 mg/mL) and the corresponding differential spectrum. The spectral changes obtained with $ZnCl_2$ titration did not resemble those obtained with ZnO and Cu-ZnO. This result was expected because the experimental conditions of pH (~6.0) and temperature differ significantly from those used by Muthumariappan, 2013 for the formation of the CIPRO-zinc complex using zinc salt[16]. Therefore, the results indicate the formation of a CIPRO-Zn complex from the etching of ZnO and Cu-ZnO. Another control experiment was performed to investigate the contribution of

CIPRO-promoted ZnO nanoetching to the formation of the CIPRO-Zn complex. In this experiment, 0.12 mg/mL of ZnO was centrifuged twice at 14,000 rpm to sediment the ZnO rice grain-like nanorods. The supernatant from the second centrifugation step was removed, CIPRO (0.02 mg/mL) was added, and the spectrum was compared with that of the CIPRO aqueous solution (Figure 5C and inset). Under these conditions, the spectral changes were consistent with the partial conversion of CIPRO to the zinc complex. Taken together, these results suggest that CIPRO formed a complex with Zn^{2+} by chelating ions previously liberated from the material surfaces, as well as by promoting nanoetching of the material surfaces.

The zeta potential values of ZnO as-synthesized and ZnO precipitated after incubation with CIPRO were -1.8 and -3.2 mV,
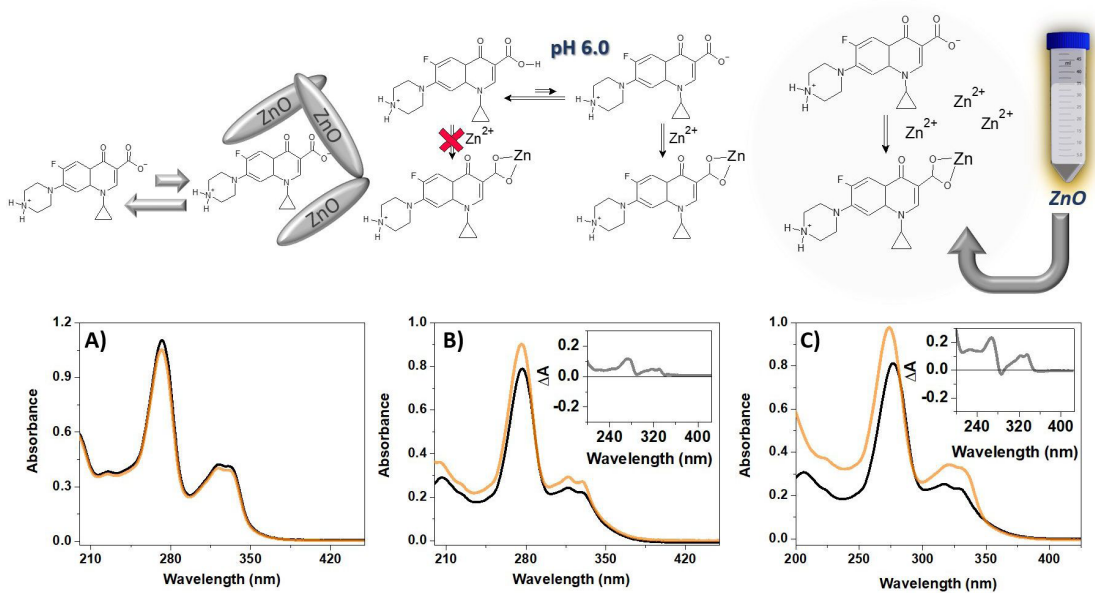
Figure 5. Binding of CIPRO on ZnO crystal surface and complexation with Zn^{2+}. A) Spectra of CIPRO titrated with ZnO before (black) and after (yellow) centrifugation at 14,000 rpm. B) Spectra of CIPRO before (black) after addition of 0.20 mg/mL of $ZnCl_2$ at pH 6.0 (yellow). C) Spectra of CIPRO aqueous solution (black) and in the supernatant of a colloidal suspension of ZnO after two centrifugations at 14,000 rpm (yellow).
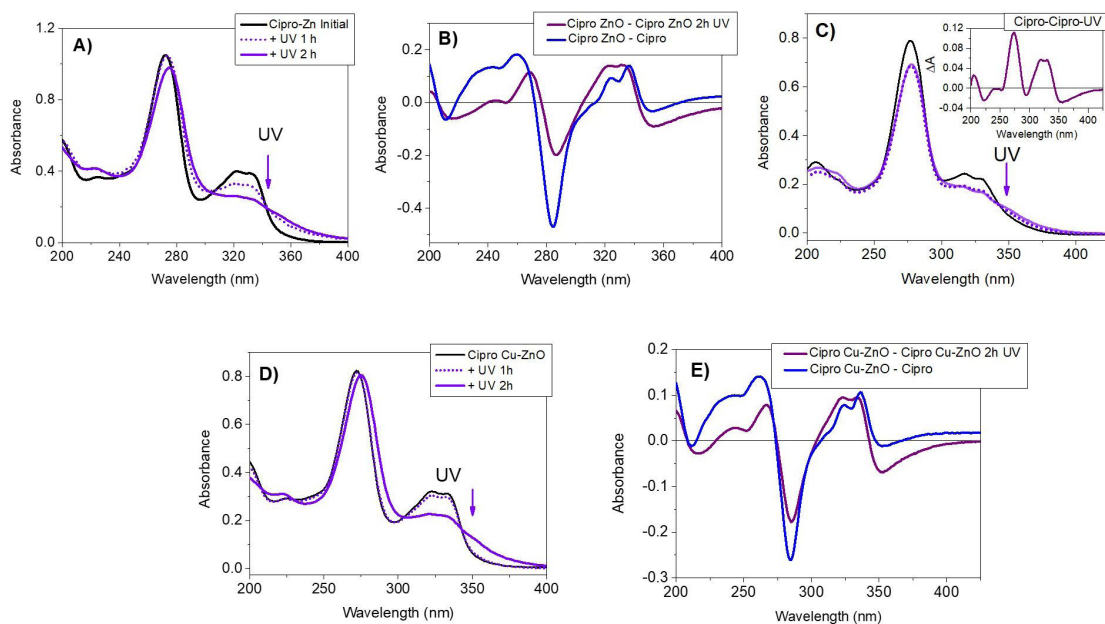

Figure 6. Photodegradation of CIPRO. A) Photobleaching of CIPRO-Zn complex obtained with ZnO and promoted by UV irradiation in two steps of 1 h as indicated by the arrow, B) Differential spectra obtained by subtracting CIPRO-Zn spectrum after 2 h of UV irradiation from the initial spectrum before irradiation (violet) and overlayed with the differential spectra of CIPRO-Zn minus CIPRO (blue). C) Photobleaching of CIPRO aqueous solution promoted by UV irradiation in two steps of 1 h as indicated by the arrow with the corresponding differential spectrum in the inset, D) Photobleaching of CIPRO-Zn complex obtained with Cu-ZnO and promoted by UV irradiation in two steps of 1 h as indicated by the arrow, E) Differential spectra obtained by subtracting CIPRO-Zn spectrum after 2 h of UV irradiation from the initial spectrum before irradiation (violet) and overlayed with the differential spectra of CIPRO-Zn minus CIPRO (blue).

respectively. The changes in the zeta potential of ZnO exposed to CIPRO were consistent with the etching of Zn^{2+} ions from the ZnO microstructure surfaces[49]. Considering that CIPRO interacted with ZnO and Cu-ZnO, promoting the etching of Zn^{2+} by complexation with the ions rather than by binding to the nanocrystals, it was important to investigate the effects

of these events on CIPRO photodegradation. We compared the photobleaching of CIPRO in the ZnO and Cu-ZnO suspensions and CIPRO in an aqueous solution exposed to UV irradiation (Figure 6A-E). The CIPRO-Zn chelate exhibited time-dependent photobleaching under UV irradiation. Photobleaching was pronounced in the broad band in the

region of 320 nm, whereas the band at 271 nm was redshifted to 276 nm (Figure 6A). This redshift may be associated with the partial zinc release of zinc. Therefore, the differential spectrum obtained by subtracting the CIPRO-Zn spectrum after 2 h of UV irradiation from the initial spectrum before irradiation was overlaid with the differential spectra of the CIPRO-Zn complex minus the CIPRO spectrum (Figure 6B). The comparison of the differential spectra suggests that photo-oxidative changes in CIPRO molecules can result in a partial loss of the chelating capacity. The CIPRO-Zn photodegradation was compared with that of pristine CIPRO (Figure 6C). CIPRO prepared in ultra-pure water exhibited significant photodegradation after 1 h of irradiation, which was not significantly increased after more than 1 h of additional irradiation. In the case of Cipro-Zn produced by incubation with Cu-ZnO, significant photodegradation was observed only after 2 h of UV irradiation (Figure 6 D).

Future kinetic studies will be necessary to determine the effect of doped and non-doped ZnO on CIPRO photodegradation. The photodegradation of CIPRO in the absence of another photosensitization indicated that CIPRO was the source and target of the reactive species. Normally, organic photosensitizers such as methylene blue[50], phenothiazines[51] and porphyrins[52] produce electronically excited species by mechanisms type II and I. Mechanism type II consists of the transfer of electronic excitation energy from the photosensitizer to molecular oxygen, generating singlet molecular oxygen $O_2 (^1\Delta_g)$, a highly reactive species. Mechanism type I involves the aggregation of photosensitizers with the generation of free radicals. Phototoxicity has been reported for fluoroquinolones; however, the magnitudes of

$O_2(^1\Delta_g)$ and superoxide ion generation by these compounds do not appear to be sufficient to explain this side effect in patients treated with these drugs[53]. It was proposed that photoinduced loss of the fluor atom as fluoride and the associated generation of a highly reactive carbene at carbon 8 could better explain phototoxicity.

Therefore, CIPRO photobleaching should involve reactions between electronically excited and radical species of fluoroquinolones. The CIPRO and CIPRO-Zn photodegradation was also analyzed by FTIR (Figure 7 A and B). The FTIR signals obtained for CIPRO originate from the functional groups present in its molecular structure, as indicated by the insets of Figure 7. The spectral shifts observed in the FTIR spectra in different conditions are also related to the effects on ICT (intramolecular charge transfer) as commented before[40,41]. The spectrum of CIPRO powder (Figure 7A, gray dotted line) is in accordance with previous report, with the presence of peaks at 3532, 3373, 3089, 2922, 2682, 2620, 1702, 1623, 1492, 1446, 1383, 1342, and 1267 cm^{-1} [54]. In the region of 1800-1200 cm^{-1}, the same vibration energy is detected in the hydrated powder, with some differences in the band ratios due to interaction with water. More significant differences were observed in the region of 3600 and 2800 cm^{-1} due to the additional contribution of water vibrations overlapping the bands of CIPRO.[55]In this region, similar spectra were observed for the CIPRO solution spectra in the region of 3600-2800 cm^{-1}. For the FTIR spectra of quinolones, the most informative region was in the range of 1800–1300 cm^{-1}. In Figure 7A, the characteristic band peaking in the 1700-1720 cm^{-1} region, which is assigned to the carbonylic vibration of the carboxylic group in ciprofloxacin hydrochloride
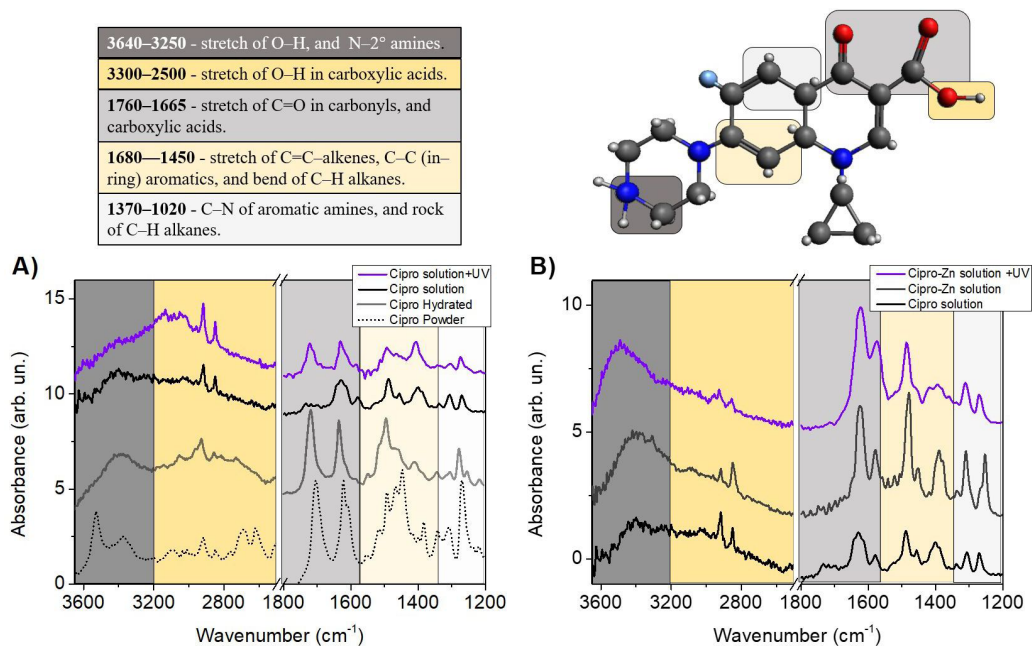

Figure 7. FTIR spectra of CIPRO exposed to UV irradiation under different conditions. A) FTIR spectra of CIPRO as powder (gray dotted line), paste (gray line), aqueous solution, and in aqueous solution after UV-irradiation (violet line); B) FTIR spectra of CIPRO aqueous solution (black line), as Zn complex before (gray line) and after 2 h of UV irradiation (violet line). The spectra panels are colored to a delimited spectral range associated to vibrations of the functional groups. In the molecular structure of CIPRO, the functional groups are indicated by the corresponding color.
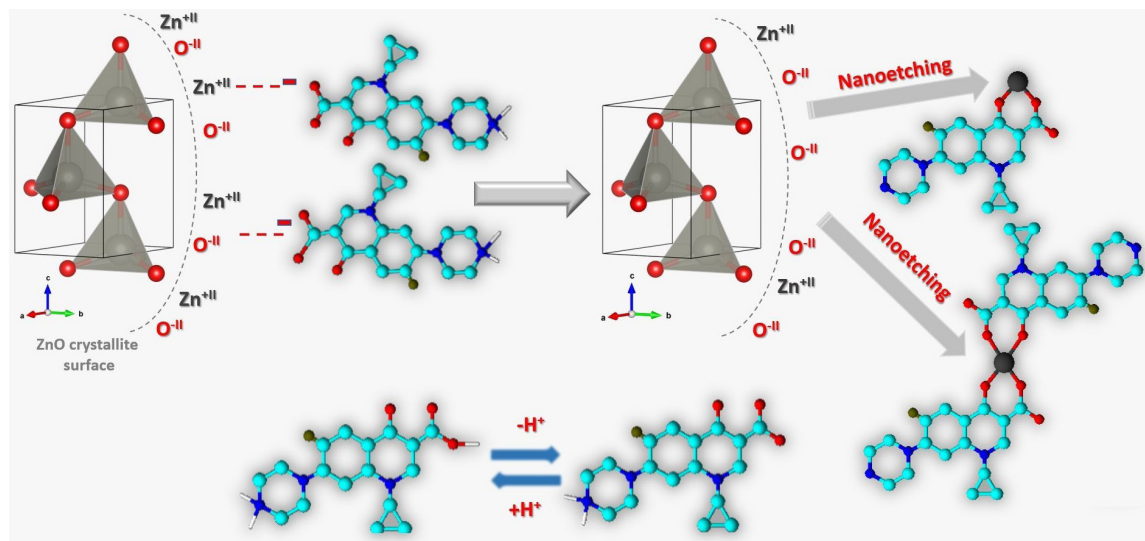
Figure 8. Formation of CIPRO-Zn complexes by nanoetching of ZnO surfaces. ZnO suspension promotes alkalinization of pure water to 7.9 that is above CIPRO pI (7.14). The unprotonated carboxylic group and the carbonyl group and pyridone carbonyl form a bidentate complex with Zn^{2+} that can coordinate with another CIPRO molecule forming a 2:1 CIPRO-Zn complex.

hydrate, was observed[55,56]. This band is intense in the spectra of the CIPRO powder and paste but absent in the CIPRO aqueous solution spectrum. This result is in accordance with other studies reporting the absence of carboxylate carbonyl bands around 1700 cm^{-1}, but instead, only the contributions of (v_{as}(O–C–O)) and symmetric (v_s(O–C–O)) stretching vibrations in the ranges of 1650–1550 cm^{-1} and 1400–1280 cm^{-1}, respectively. Contributions from overlapped bands peaking at approximately 1640, 1630 and 1610 cm^{-1} were observed in the CIPRO solution spectrum. The CIPRO solution spectrum also exhibits a broad band in the 1412-1380 cm^{-1} region and defined bands at 1307 and 1275 cm-1. In the spectra of CIPRO photobleached by 2 h of irradiation with UV light, the contribution at 1700 cm^{-1} is now present and appears as a composite band resulting from contributions around 1740 (shoulder), 1722 and 1710 (shoulder) cm^{-1}. This result suggests the formation of diverse photoproducts that retain the original CIPRO carboxylic group. It is also possible to form new carboxylic groups in the photoproducts because of oxidative modifications. Significant changes were also observed in the spectral ranges of 1630, 1480 and 1270 cm^{-1}. It is important to note that a significant decrease in the signal around 1618 cm^{-1} was observed in the spectrum of CIPRO photobleached by UV. The band at 1618 cm^{-1} was assigned to the stretching vibration of the pyridone functional group[55,56]. Figure 7B compares the spectra of CIPRO, CIPRO-Zn and CIPRO-Zn photobleached by UV irradiation. Consistent with the spectral changes observed in the absorbance spectra, significant changes were observed in the carbonyl groups of CIPRO-Zn, which are the groups involved in coordination with Zn^{2+}. In the region of 1600-1200 cm^{-1}, the spectra of CIPRO and CIPRO-Zn were similar. In the spectrum of CIPRO-Zn subjected to 2h of UV irradiation, the most pronounced changes were observed in the bands at 1623 and 1580 cm^{-1}, which broadened, suggesting the formation of derivatives that remained coordinated with Zn^{2+}. The bands in the 1440-1340 cm^{-1} range of photobleached CIPRO-Zn

showed a significant decrease. Therefore, absorbance and FTIR spectroscopy demonstrated that both CIPRO and CIPRO-Zn were susceptible to UV-promoted photodegradation. However, it is not possible to ascertain whether, under the present conditions, CIPRO and CIPRO-Zn were converted to different photoproducts. Quinolones present FTIR with numerous overlapping bands that make it difficult to ascribe their vibrations unequivocally[55].

4. Conclusion

To produce a low-cost material, with good biocompatibility for CIPRO photodegradation, ZnO and Cu-ZnO were synthesized and used without annealing. Although without thermal treatment, the XRD measurements showed that the materials have a high degree of crystallinity. The synthesis method, without a calcination step, results in the presence of zinc oxyhydroxide (or zinc hydroxide hydrate phase), which could be the cause of the low degree of adsorption estimated in ~4% of CIPRO on the material surfaces. The presence of a hydrated phase at the interface with water led to the release of zinc ions in the medium and favored the etching of the material surface by Cipro, as illustrated in Figure 8. $ZnCl_2$ cannot efficiently substitute ZnO to produce Cipro chelates because this salt does not alkalize the medium.

Thus, in the presence of ZnO and Cu-ZnO, the formation of Cipro-Zn chelates occurred, which are desirable species because they prevent bacterial selection for resistance[57]. In addition, CIPRO-Zn exhibited efficient photodegradation under UV light exposure. In the next stage of investigation, we intend to invest in a nanostructured thermally treated material under different temperatures to optimize its surface dynamics, binding affinity and photoactivity of ZnO for cipro removal and degradation. The annealed nanostructured form has fewer defects and a considerable increase in the surface area, in which the photoactivated surface reactions are driven.

5. Acknowledgements

6. References

1. Sharma PC, Jain A, Jain S, Pahwa R, Yar MS. Ciprofloxacin: review on developments in synthetic, analytical, and medicinal aspects. J Enzyme Inhib Med Chem. 2010;25(4):577-89.

2. Caço AI, Varanda F, Pratas de Melo MJ, Dias AMA, Dohrn R, Marrucho IM. Solubility of antibiotics in different solvents. Part II. Non-hydrochloride forms of tetracycline and ciprofloxacin. Ind Eng Chem Res. 2008;47(21):8083-9.

3. Mella M, Fasani E, Albini A. Photochemistry of 1-Cyclopropyl-6-fluoro-1,4-dihydro-4-oxo-7- (piperazin-1-yl)quinoline-3-carboxylic Acid (=Ciprofloxacin) in Aqueous Solutions. Helv Chim Acta. 2001;84(9):2508-19.

4. Albini A, Monti S. Photophysics and photochemistry of fluoroquinolones. Chem Soc Rev. 2003;32(4):238-50.

5. Van Doorslaer X, Demeestere K, Heynderickx PM, Van Langenhove H, Dewulf J. UV-A and UV-C induced photolytic and photocatalytic degradation of aqueous ciprofloxacin and moxifloxacin: reaction kinetics and role of adsorption. Appl Catal B. 2011;101(3-4):540-7.

6. Bani-Yaseen AD, Hammad F, Ghanem BS, Mohammad EG. On the photophysicochemical properties of selected fluoroquinolones: solvatochromic and fluorescence spectroscopy study. J Fluoresc. 2013;23(1):93-101.

7. Lorenzo F, Navaratnam S, Allen NS. Formation of secondary triplet species after excitation of fluoroquinolones in the presence of relatively strong bases. J Am Chem Soc. 2008;130(37):12238-9.

8. Cuquerella MC, Andreu I, Soldevila S, Bosca F. Triplet excimers of fluoroquinolones in aqueous media. J Phys Chem A. 2012;116(21):5030-8.

9. Kim T-K, Kim T, Park H, Lee I, Jo A, Choi K, et al. Degradation of ciprofloxacin and inactivation of ciprofloxacin resistant E. faecium during UV-LED (275 nm)/chlorine process. Chem Eng J. 2020;394:124803.

10. Guo HG, Gao NY, Chu WH, Li L, Zhang YJ, Gu JS, et al. Photochemical degradation of ciprofloxacin in UV and UV/H2O2 process: Kinetics, parameters, and products. Environ Sci Pollut Res Int. 2013;20(5):3202-13.

11. Yu X, Zhang J, Zhang J, Niu J, Zhao J, Wei Y, et al. Photocatalytic degradation of ciprofloxacin using Zn-doped Cu2O particles: analysis of degradation pathways and intermediates. Chem Eng J. 2019;374:316-27.

12. Cleuvers M. Initial risk assessment for three β-blockers found in the aquatic environment. Chemosphere. 2005;59(2):199-205.

13. Frade VMF, Dias M, Teixeira ACSC, Palma MSA. Environmental contamination by fluoroquinolones. Braz J Pharm Sci. 2014;50(1):41-54. http://dx.doi.org/10.1590/s1984-82502011000100004.

14. Zhang QQ, Ying GG, Pan CG, Liu YS, Zhao JL. Comprehensive evaluation of antibiotics emission and fate in the river basins of China: source analysis, multimedia modeling, and linkage to bacterial resistance. Environ Sci Technol. 2015;49(11):6772-82.

15. Wang Q, Wang P, Yang Q. Occurrence and diversity of antibiotic resistance in untreated hospital wastewater. Sci Total Environ. 2018;621:990-9.

16. Muthumariappan S. Synthesis and characterization of ciprofloxacin–zinc (II) complex and assay studies in pharmaceutical drugs. J Pharm Res. 2013;6(4):437-41.

17. Liao X, Li B, Zou R, Dai Y, Xie S, Yuan B. Biodegradation of antibiotic ciprofloxacin: pathways, influential factors, and bacterial community structure. Environ Sci Pollut Res Int. 2016;23(8):7911-8.

18. Beegam A, Prasad P, Jose J, Oliveira M, Costa FG, Soares AMVM, et al. Environmental fate of zinc oxide nanoparticles: risks and benefits. In: Larramendy ML, Soloneski S, editors. Toxicology - new aspects to this scientific conundrum. London: InTech; 2016. http://dx.doi.org/10.5772/65266.

19. Dong S, Feng J, Fan M, Pi Y, Hu L, Han X, et al. Recent developments in heterogeneous photocatalytic water treatment using visible light-responsive photocatalysts: a review. RSC Advances. 2015;5(19):14610-30.

20. Liu H, Wang C, Wang G. Photocatalytic advanced oxidation processes for water treatment: recent advances and perspective. Chem Asian J. 2020;15(20):3239-53.

21. Ameta R, Solanki MS, Benjamin S, Ameta S. Photocatalysis. In: Ameta SC, Ameta R, editors. Advanced oxidation processes for wastewater treatment: emerging green chemical technology. USA: Elsevier Inc.; 2018. p. 135-75. http://dx.doi.org/10.1016/B978-0-12-810499-6.00006-1.

22. Nosaka Y, Nosaka A. Understanding hydroxyl radical (•OH) Generation Processes in Photocatalysis. ACS Energy Lett. 2016;1(2):356-9.

23. Bessegato GG, Guaraldo TT, de Brito JF, Brugnera MF, Zanoni MVB. Achievements and Trends in Photoelectrocatalysis: from Environmental to Energy Applications. Electrocatalysis. 2015;6(5):415-41.

24. Yang Q, Lin TS, Burton C, Park SH, Ma Y. Physicochemical insights of irradiation-enhanced hydroxyl radical generation from ZnO nanoparticles. Toxicol Res (Camb). 2015;5(2):482-91.

25. He W, Wu H, Wamer WG, Kim HK, Zheng J, Jia H, et al. Unraveling the enhanced photocatalytic activity and phototoxicity of ZnO/metal hybrid nanostructures from generation of reactive oxygen species and charge carriers. ACS Appl Mater Interfaces. 2014;6(17):15527-35.

26. Rao MV, Rajeshwar K, Verneker VRP, DuBow J. Photosynthetic production of hydrogen and hydrogen peroxide on semiconducting oxide grains in aqueous solutions. J Phys Chem. 1980;84(15):1987-91.

27. He W, Jia H, Cai J, Han X, Zheng Z, Wamer WG, et al. Production of reactive oxygen species and electrons from photoexcited zno and zns nanoparticles: a comparative study for unraveling their distinct photocatalytic activities. J Phys Chem C. 2016;120(6):3187-95.

28. Menezes LR, Lopes DM, Bronzato JD, Sombrio G, Criado D, Zuniga A, et al. Photo-induced Electron Transfer from Hematite and Zinc Oxide Nanostructures to Cytochrome C: Systems Applicable to Spintronics. In: 2019 IEEE 9th International Nanoelectronics Conferences (INEC); 2019; July 3-5; Kuching, Malaysia. Proceedings. USA: IEEE; 2019. p. 1-9.

29. Menezes LR, Chaves JCA, Lopes DM, Bronzato JD, Sombrio G, Criado D, et al. Effect of the protein structure and heme iron coordination sphere on the long-range electron transfer from hematite and zinc oxide nanostructures to cytochrome c. Int J Nanotechnol. 2020;17(1):42-56.

30. Domènech X, Ayllón JA, Peral J. H2O2 formation from photocatalytic processes at the ZnO/water interface. Environ Sci & Pollut Res. 2001;8:285-7.

31. Janotti A, Van de Walle CG. Fundamentals of zinc oxide as a semiconductor. Rep Prog Phys. 2009;72(12):126501.

32. Muruganandham M, Zhang Y, Suri R, Lee GJ, Chen PK, Hsieh SH, et al. Environmental applications of ZnO materials. J Nanosci Nanotechnol. 2015;15(9):6900-13.

33. Sajjad M, Ullah I, Khan MI, Khan J, Khan MY, Qureshi MT. Structural and optical properties of pure and copper doped zinc oxide nanoparticles. Results Phys. 2018;9:1301-9.

34. Niranjan K, Dutta S, Varghese S, Ray AK, Barshilia HC. Role of defects in one-step synthesis of Cu-doped ZnO nano-coatings by electrodeposition method with enhanced magnetic and electrical properties. Appl Phys, A Mater Sci Process. 2017;123(4):250.

35. Zhao W, Song X, Chen G, Sun S. Hydrothermal synthesis of hollow twinning ZnO microstructures. Cryst Res Technol. 2009;44(4):373-8.

36. Santos HF, dos Santos CG, Nascimento OR, Reis AKCA, Lanfredi AJC, de Oliveira HPM, et al. Charge separation of photosensitized phenothiazines for applications in catalysis and nanotechnology. Dyes Pigments. 2020;177:108314.

37. Dabir F, Esfahani H, Bakhtiargonbadi F, Khodadadi Z. Study on microstructural and electro-optical properties of sol–gel derived pure and Al/Cu-doped ZnO thin films. J Sol-Gel Sci Technol. 2020;96(3):529-38.

38. Bhardwaj R, Bharti A, Singh JP, Chae KH, Goyal N. Influence of Cu doping on the local electronic and magnetic properties of ZnO nanostructures. Nanoscale Adv. 2020;2:4450-63. http://dx.doi.org/10.1039/d0na00499e.

39. Mohan R, Krishnamoorthy K, Kim SJ. Enhanced photocatalytic activity of Cu-doped ZnO nanorods. Solid State Commun. 2012;152(5):375-80.

40. Lokesh B, Rao NM. Effect of Cu-doping on structural, optical and photoluminescence properties of zinc titanates synthesized by solid state reaction. J Mater Sci Mater Electron. 2016;27(5):4253-8.

41. Chow L, Lupan O, Chai G, Khallaf H, Ono LK, Roldan Cuenya B, et al. Synthesis and characterization of Cu-doped ZnO one-dimensional structures for miniaturized sensor applications with faster response. Sens Actuators A Phys. 2013;189:399-408.

42. Snopok BA, Zavyalova LV, Tatyanenko NP, Gudymenko AI, Svechnikov GS, Kladko VP, et al. The effect of small addition of copper on the growth process, structure, surface charge and adsorption properties of ZnO films in the pyrolysis of dithiocarbamates. Mater Adv. 2021;2(11):3637-54.

43. Xu DH, Shen WZ. Cu-Doped ZnO hemispherical shell structures: synthesis and room-temperature ferromagnetism properties. J Phys Chem C. 2012;116(24):13368-73.

44. Pawar RC, Choi D-H, Lee J-S, Lee CS. Formation of polar surfaces in microstructured ZnO by doping with Cu and applications in photocatalysis using visible light. Mater Chem Phys. 2015;151:167-80.

45. Zhu L, Li H, Liu Z, Xia P, Xie Y, Xiong D. Synthesis of the 0D/3D CuO/ZnO Heterojunction with Enhanced Photocatalytic Activity. J Phys Chem C. 2018;122(17):9531-9.

46. Sarkar S, Basak D. Defect controlled ultra high ultraviolet photocurrent gain in Cu-doped ZnO nanorod arrays: de-trapping yield. Appl Phys Lett. 2013;103(4):041112.

47. Licurgo JSC, de Almeida GR No, Paes HR Jr. Structural, electrical and optical properties of copper-doped zinc oxide films deposited by spray pyrolysis. Ceramica. 2020;66(379):284-90.

48. Moradi-e-Rufchahi EO, Ghanadzadeh A. A study of Solvatochromism in diazonium coupling products of 6-flouro 4-hydroxyl-2-quinolone. J Mol Liq. 2011;160(3):160-5.

49. Meinderink D, Kielar C, Sobol O, Ruhm L, Rieker F, Nolkemper K, et al. Effect of PAA-induced surface etching on the adhesion properties of ZnO nanostructured films. Int J Adhes Adhes. 2021;106:102812.

50. Estevam ML, Nascimento OR, Baptista MS, Di Mascio P, Prado FM, Faljoni-Alario A, et al. Changes in the spin state and reactivity of cytochrome c induced by photochemically generated singlet oxygen and free radicals. J Biol Chem. 2004;279(38):39214-22.

51. dos Santos CG, Silva AL, Souza FL, Lanfredi AJ, Di Mascio P, Nascimento OR, et al. UV-Light effects on cytochrome C modulated by the aggregation state of phenothiazines. PLoS One. 2013;8(10):e76857.

52. Kawai C, Araújo-Chaves JC, Magrini T, Sanches CO, Pinto SM, Martinho H, et al. Photodamage in a mitochondrial membrane model modulated by the topology of cationic and anionic meso-tetrakis porphyrin free bases. Photochem Photobiol. 2014;90(3):596-608.

53. Martinez LJ, Sik RH, Chignell CF. Fluoroquinolone antimicrobials: singlet oxygen, superoxide and phototoxicity. Photochem Photobiol. 1998;67(4):399-403.

54. Bhongade B, Talath S, Dhaneshwar S. A validated method for the quantitation of ciprofloxacin hydrochloride using diffuse reflectance infrared fourier transform spectroscopy. Int J Spectrosc. 2014;2014:1-6.

55. Zupančič M, Turel I, Bukovec P, White AJP, Williams DJ. Synthesis and characterization of two novel zinc(II) complexes with ciprofloxacin. Crystal structure of [C17H19N3O3F]2 · [znCl4] · 2H2O. Croat Chem Acta. 2001;74(1):61-74.

56. Turel I, Leban I, Bukovec N. Crystal structure and characterization of the bismuth(III) compound with quinolone family member (ciprofloxacin). Antibacterial study. J Inorg Biochem. 1997;66(4):241-5.

57. Vos M, Sibleyras L, Lo LK, Hesse E, Gaze W, Klümper U. Zinc can counteract selection for ciprofloxacin resistance. FEMS Microbiol Lett. 2020;367(3):fnaa038. http://dx.doi.org/10.1093/femsle/fnaa038.

Supplementary material

The following online material is available for this article:

Supplementary Material